Supplementary Materials

Highly Effective Solid Solution towards High Thermoelectric and Mechanical Performance in Bi-Sb-Te Alloys via Trojan Doping

Yong-Cai Shi[1#], Jianmin Yang[2#], Yu Wang[1#], Zu-Gang Li[1], Tian-Yu Zhong[1], Zhen-Hua Ge[1], Jing Feng[1*] and Jiaqing He[2*]*

1 Faculty of Materials Science and Engineering, Kunming University of Science and Technology, Kunming, 650093, China.

2 Shenzhen Key Laboratory of Thermoelectric Materials, Department of Physics, Southern University of Science and Technology, Shenzhen, 518055, China

**Corresponding author. E-mail: Z.-H. Ge (zge@kmust.edu.cn) J. Feng (jingfeng@kust.edu.cn), J. He (hejq@sustech.edu.cn)*

Supplementary Figure

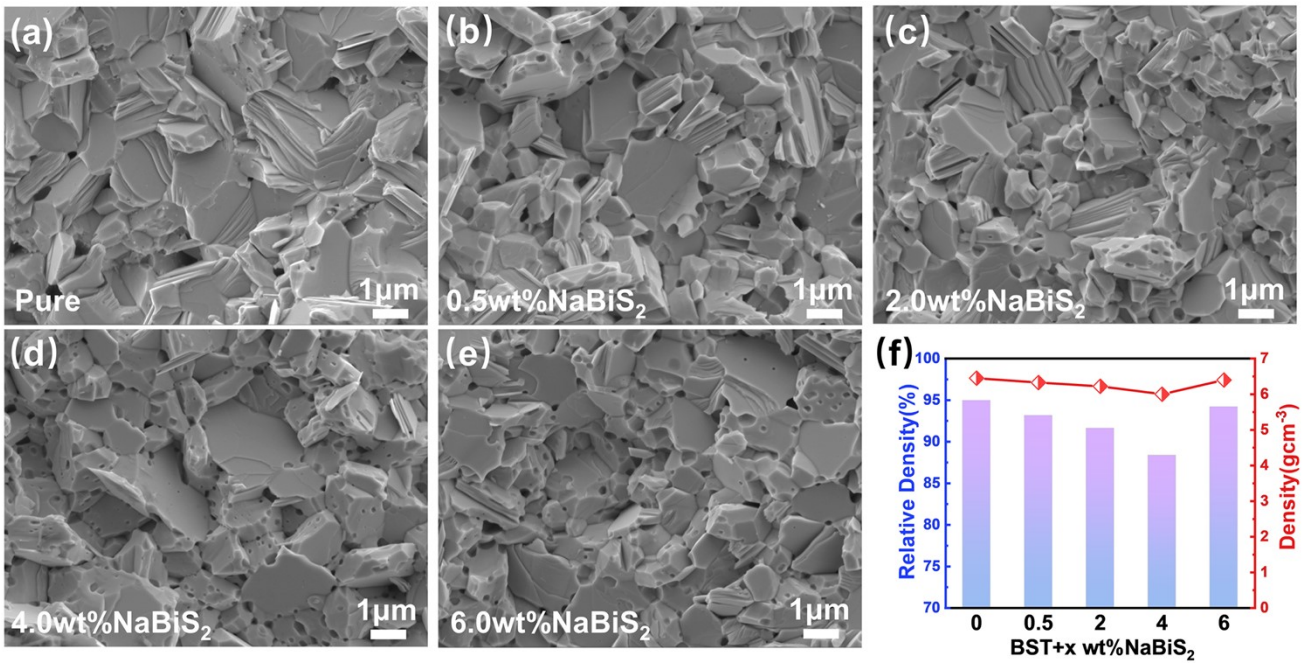

Figure S1 SEM images of different $NaBiS_2$ doping contents, showing their micro-morphological features at the micron scale. (f) the variation of density and relative density with $NaBiS_2$ doping content.

Experiment Details

$NaBiS_2$ Nanoribbons Synthesis: All chemical reagents directly used in this work were analytical-grade materials without further purification. The $NaBiS_2$ powders were fabricated, starting with commercial $Bi(NO_3)_3 \cdot 5H_2O$ and $Na_2S \cdot 9H_2O$ as raw materials. First, $Bi(NO_3)_3 \cdot 5H_2O$ (3.75 mmol) and Na_2S $9H_2O$ (15.6 mmol) were dissolved into 25mL deionized water (DI) and 50mL ethylene glycol (EG), respectively, and then the sodium sulfide solution was slowly added into bismuth nitrate solvent and heated at 100 C, stirring for 10 min before NaOH (2 g) was added to the mixture. The final black solid product was washed with DI water six times with centrifugation (3500 rpm) and then with ethanol three times more, followed by drying under a vacuum at 120 C for 12h. The phase structure and microscopic morphology of the $NaBiS_2$ nanoribbons can be found in our previous work. [1]

X-ray diffraction (XRD) analysis was utilized to identify the crystal structure of the samples. The XRD patterns were obtained using a MiniFlex600 (Rigaku, Japan) diffractometer with Cu Kα radiation (λ = 1.5406 Å), and the diffraction patterns were collected within a 2θ range of 20-70° with a step size of 0.01°. The electrical performance was tested using the ZEM3 Seebeck/resistance test system produced by Company Ulvac-Riko, Japan. The thermal conductivity can be obtained from the equation $\boldsymbol{\kappa}=\boldsymbol{\rho}\cdot\boldsymbol{D}\cdot\boldsymbol{C_p}$, where the density is obtained from the commonly used Archimedes method. The thermal diffusion coefficient $\boldsymbol{D}$ was measured using an LFA467 produced by the German Netzsch Company. The uncertainty of the Seebeck coefficient and electrical conductivity measurements was 5%. The uncertainty of the thermal conductivity was estimated to be within 8%, considering the uncertainties from D, Cp, and ρ. The combined uncertainty for all measurements involved in the calculation of ZT was less than 20%. The sample size for thermal conductivity testing was 6×6 mm, with a thickness of approximately 1.0 mm. The carrier concentration and mobility were measured using the Hall coefficient tester (PPMS-9T, Quantum Design Inc., USA), while the velocity of sound was measured by the ultrasonic reflection method (UMS-100, TECLAB, France). The grain morphology and microstructure of the bulk materials were characterized using field emission scanning electron microscopy (ZEISS, Sigma 300, Germany). The mechanical properties, Vickers hardness,and Young's modulus were measured using nanoindentation method (iMicro KLA., USA).

TEM samples were prepared using the traditional method. The original bulk specimens were polished to ~40 μm and further thinned to be electron-transparent in a precision ion polishing system at a small angle (5°). Major milling was performed with a 3.5 kV ion beam. Final milling to minimize

the damage layer on the region of interest was performed with 0.2 kV and 0.1 kV ion beams. Structure characterization by TEM was performed with a Thermo Fisher Scientific Themis G2 60-300 in STEM mode. All the observations in this work are under 300 kV.

Sing-leg thermoelectric device fabrication and power generation performance measurement

The power generation performance of the single-leg device was tested using the Mini-PEM from Advance Riko. We selected the 4.0 wt.% $NaBiS_2$ doped sample as the single-leg device particle, and then prepared the contacting layer (Ni) on the upper and lower surfaces of the sample by electroplating. In order to further reduce the contact resistance at the interface, silver pastes were added between the Cu sheet and the Ni layer as a connecting layer. Before welding, we used 2000-mesh sandpaper to slightly polish the copper electrode to increase the bonding force between the electrode and the thermoelectric particles. The schematic structure of the single-leg device used in the final test is shown in **Fig. S2**. The prepared single-leg thermoelectric device was set up on the Mini-PEM instrument (Illustration of Fig. 6c), and silicone grease was applied to the Cu sheet at the high-temperature end to improve thermal conductivity. The test temperature difference was set to 50 K, 100 K, 150 K, 200 K and 250 K, and the cold end temperature was set to ~ 295 K. The measurement results were provided in terms of output voltage, output power density, and conversion efficiency (Fig. 6c, d).

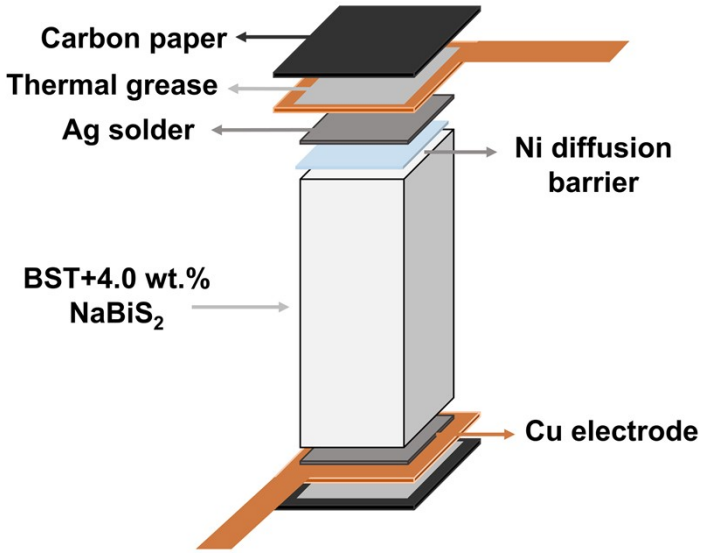

Figure S2 Schematic structure of TE single-leg device prepared from 4.0 wt.% $NaBiS_2$ doped sample.

Computational details

The first-principle calculations were performed by utilizing the Perdew-Burke-Ernzerhof (PBE) formalism and generalized gradient approximation (GGA) implemented in Vienna ab initio simulation package (VASP) code[2]. To simulate the substituted impurities, we have used a 3×3×3 supercell containing 135 atoms. An energy cutoff of 400 eV was used. All geometry structures were fully relaxed until the calculated Hellmann-Feynman force on every atom was less than 0.01 eV $Å^{-1}$ under the convergence condition of 10^{-4} eV. Due to the presence of heavy elements Bi, Sb, Te, all calculations take into account the spin-orbit coupling effect (SOC).

Defect formation energy calculation.

This work uses the first-principles defect calculations with density functional theory (DFT) to explore the native defects. The formation enthalpies of point defect (**ΔE**) are defined as following[3-6]:

$$\Delta E_q = E_{defect,q} - E_{perfect} - \sum_i n_i \mu_i + q(E_f + E_V + \Delta V) + E_{corr}$$

Where the term $E_{defect,\,q}$ and $E_{perfect}$ are the total energy of the defect-free host crystal and the host crystal with defect D in charge state $\boldsymbol{q}$. The $\mathbf{n_i}$ and $\boldsymbol{\mu_i}$ are the number and the chemical potentials of type i elements. The $\mathbf{n_i} > 0$and $\mathbf{n_i} < 0$ represent that the atom i is added to and removed from the supercell, respectively. $\boldsymbol{E_F}$ and $\boldsymbol{E_V}$ are Fermi energy and the energy of VBM. $\boldsymbol{\Delta V}$ is denoted as the averaged difference between the local potential far from the defect in the defective supercell and the corresponding one in the perfect supercell. Ecorr is the image charge corrections in a charged supercell, which is calculated by the Lany and Zunger correction method in this work. In this work, only the formation energy of neutral atoms is considered, so the following formula is obtained.

$$\Delta E = E_{defect} - E_{perfect} - \sum_i n_i \mu_i + E_{corr}$$

where μ_i is the chemical potential of the atom, which mainly depends on the prepared chemical environment.

Crystal orbitals Hamiltonian population (-pCOHP)

To further understand the chemical bonding, we performed projected crystal orbitals Hamiltonian population (-pCOHP) analysis between S, Te, and Na. We use the ***lobster*** software package to analyze the chemical-bonding interaction. The -pCOHP of the optimized structure and the DFT calculation were calculated

Calculation of the lattice thermal conductivity via the Debye-Callaway model

According to the extensively applied Debye-Callaway model, the lattice thermal conductivity has the following expression [7-12]

$$\kappa_{lat} = \frac{k_B}{2\pi^2 v}\left(\frac{k_B T}{\hbar}\right)^3 \int_0^{\theta_D/T} \tau_{tot}(x)\frac{x^4 e^x}{(e^x-1)^2}dx \tag{S1}$$

where x is defined as $\hbar\omega/kT_B$, $\hbar$ is the reduced Plank constant, ω is the phonon frequency, v is the average phonon velocity, and θ_D is Debye temperature. τ_{tot} is the total relaxation time including the Umklapp process and normal process scattering (τ_U +τ_N), alloy scattering (τ_A), grain boundary scattering (τ_{GB}), and the scattering from dislocations (τ_{DS}) and nanoprecipitates (τ_{NP}):

$$\tau_{tot}^{-1} = \tau_U^{-1} + \tau_N^{-1} + \tau_{GB}^{-1} + \tau_A^{-1} + \tau_{DS}^{-1} + \tau_{NP}^{-1} \tag{S2}$$

the specific symbol expressions are shown below and parameters are listed in Table S1.

$$\tau_U^{-1} + \tau_N^{-1} = A_N \frac{2^{k_B}\bar{V}^{1/3}\gamma^2\omega^2 T}{(6\pi^2)^{1/3}\bar{M}v^3} \tag{S3}$$

$$\tau_{GB}^{-1} = \frac{v}{d} \tag{S4}$$

$$\tau_A^{-1} = \frac{\bar{V}\omega^4}{4\pi v^3}\Gamma \tag{S5}$$

Where T is point defect scattering parameter and can be expressed as [13]:

$$\Gamma = x(1-x)\left[\left(\frac{\Delta M}{M}\right)^2 + \frac{2}{9}\{(G+6.4\gamma)\frac{1+r}{1-r}\}^2(\frac{\Delta a}{a})^2\right] \tag{S6}$$

$$\tau_{DS}^{-1} = N_D\frac{\bar{V}^{4/3}}{v^2}\omega^3 + 0.6N_D\gamma^2 B_D^2\omega\left\{\frac{1}{2} + \frac{1}{24}\left(\frac{1-2\nu}{1-\nu}\right)^2\left[1+\sqrt{2}\left(\frac{v_L}{v_T}\right)^2\right]^2\right\} \tag{S7}$$

$$\tau_{NP}^{-1} = v(\sigma_s^{-1} + \sigma_l^{-1})^{-1} V_{NP}, with\ \sigma_s = 2\pi R^2, \sigma_l = \pi R^2 \frac{4}{9}\left(\frac{\Delta D}{D_m}\right)^2\left(\frac{\omega R}{v}\right)^4 \quad \text{(S8)}$$

$$v_a = \left[\frac{1}{3}\left(\frac{1}{v_l^3} + \frac{2}{v_t^3}\right)\right]^{-1/3} \quad \text{(S9)}$$

$$\gamma = \frac{3}{2}\left(\frac{1+v_p}{2-3v_p}\right) \quad \text{(S10)}$$

$$v_p = \frac{1 - 2\left(v_t/v_l\right)^2}{2 - 2\left(v_t/v_l\right)^2} \quad \text{(S11)}$$

Table S4. Parameters used to calculate κ_L based on various phonon scattering processes.

Parameters	Values	Methods
Average atomic mass M (kg)	2.22×10^{-25}	Ref.[7]
Average atomic mass volume V_0 (m^3)	3.13×10^{-29}	Ref.[7]
Boltzmann constant k_B (J/K)	1.38×10^{-23}	-
Grüneisen parameter γ	1.61	Eq.S9
Average sound velocity v (m/s)	1918	Eq.S8
Longitudinal velocity v_L (m/s)	3084	Exp
Transverse velocity v_T (m/s)	1723	Exp
Ratio of N- to U- processes β	2.6	Ref.[9]
Denstiy for pure BST (kg/m3)	6540	Exp
Point defect scattering parameter Γ pure BST	0.265	Eq.S6
Γ for 0.5	0.390	Eq.S6
Γ for 2.0	0.425	Eq.S6
Γ for 4.0	0.590	Eq.S6
Average grain size	1.5 μm	Exp

Reaptability test for temperature-dependent TE properties

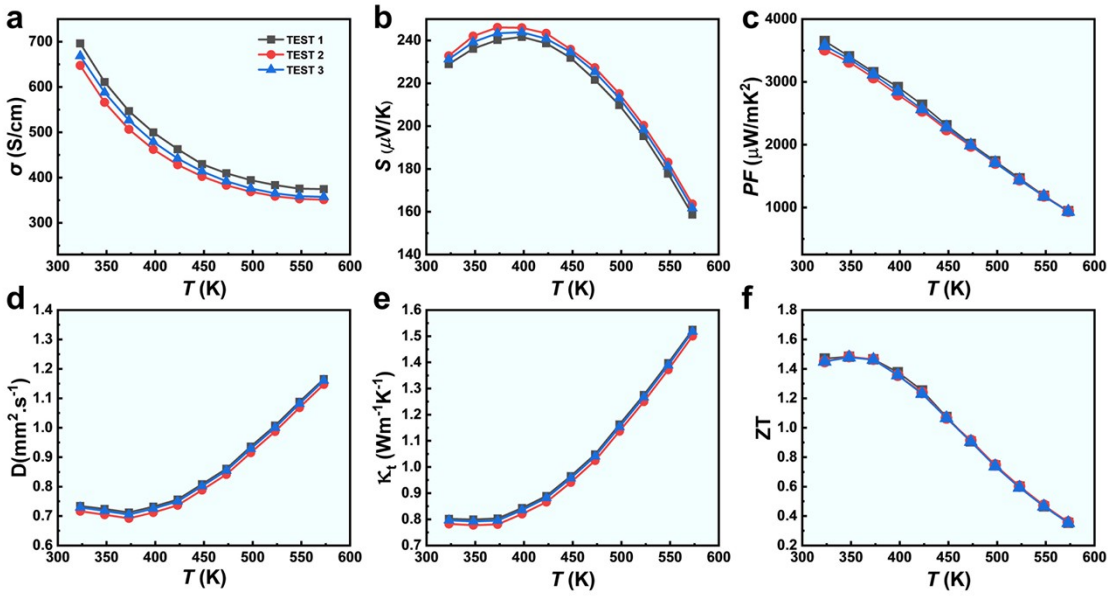

Figure S3 The repeatability test for temperature-dependent TE properties. (a) Electrical conductivity, (b) Seebeck coefficient, (c) Power Factor, (d) thermal diffusivity, (e) Total thermal conductivity, (f) *ZT*

References

[1] J. Guo, Z. H. Ge, M. Hu, P. Qin, J. Feng, Facile Synthesis of $NaBiS_2$ Nanoribbons as a Promising Visible Light-Driven Photocatalyst, Phys. Status Solidi RRL 12(9) (2018)1800135.

[2]J.P. Perdew, K. Burke, M. Ernzerhof, Generalized Gradient Approximation Made Simple, Phys. Rev. Lett. 77(18) (1996) 3865-3868.

[3] Y. Cao, H. Bai, Z. Li, Z. Zhang, Y. Tang, X. Su, J. Wu, X. Tang, Zn-Induced Defect Complexity for the High Thermoelectric Performance of n-Type PbTe Compounds, ACS Appl. Mater. Interfaces 13(36) (2021) 43134-43143.

[4] V. Karthikeyan, S.L. Oo, J.U. Surjadi, X. Li, V.C.S. Theja, V. Kannan, S.C. Lau, Y. Lu, K.H.

Lam, V.A.L. Roy, Defect Engineering Boosted Ultrahigh Thermoelectric Power Conversion Efficiency in Polycrystalline SnSe, ACS Appl. Mater. Interfaces 13(49) (2021) 58701-58711.

[5] J. Sun, R. Wang, W. Cui, S. Xie, T. Luo, H. Bai, X. Zhao, Z. Chen, X. Sang, X. Tan, X. Tang, G. Tan, Percolation Process-Mediated Rich Defects in Hole-Doped PbSe with Enhanced Thermoelectric Performance, Chem. Mater. 34(14) (2022) 6450-6459.

[6] J. Zhang, L. Song, B.B. Iversen, Improved Thermoelectric Properties of N-Type Mg_3Sb_2 through Cation-Site Doping with Gd or Ho, ACS Appl. Mater. Interfaces 13(9) (2021) 10964-10971.

[7] B. Cai, H.-L. Zhuang, J. Pei, B. Su, J.-W. Li, H. Hu, Y. Jiang, J.-F. Li, Spark plasma sintered Bi-Sb-Te alloys derived from ingot scrap: Maximizing thermoelectric performance by tailoring their composition and optimizing sintering time, Nano Energy 85 (2021) 106040.

[8] B. Chen, J. Li, M. Wu, L. Hu, F. Liu, W. Ao, Y. Li, H. Xie, C. Zhang, Simultaneous Enhancement of the Thermoelectric and Mechanical Performance in One-Step Sintered n-Type Bi_2Te_3-Based Alloys via a Facile MgB2 Doping Strategy, ACS Appl. Mater. Interfaces 11(49) (2019) 45746-45754.

[9] Y. Pan, U. Aydemir, J.A. Grovogui, I.T. Witting, R. Hanus, Y. Xu, J. Wu, C.F. Wu, F.H. Sun, H.L. Zhuang, J.F. Dong, J.F. Li, V.P. Dravid, G.J. Snyder, Melt-Centrifuged $(Bi,Sb)_2Te_3$: Engineering Microstructure toward High Thermoelectric Efficiency, Adv. Mater. 30(34) (2018) 1802016.

[10] G. Yang, R. Niu, L. Sang, X. Liao, D.R.G. Mitchell, N. Ye, J. Pei, J.F. Li, X. Wang, Ultra-High Thermoelectric Performance in Bulk BiSbTe/Amorphous Boron Composites with Nano-Defect Architectures, Adv. Energy Mater. 10(41) (2020) 2000757.

[11] G. Yang, L. Sang, F.F. Yun, D.R.G. Mitchell, G. Casillas, N. Ye, K. See, J. Pei, X. Wang, J.F. Li, G.J. Snyder, X. Wang, Significant Enhancement of Thermoelectric Figure of Merit in BiSbTe-Based Composites by Incorporating Carbon Microfiber, Adv. Functional Mater. 31(15) (2021) 2008851.

[12] C. Zhu, J. Wang, F. Luo, S. Zhang, J. Wang, Y. Zhang, H. Liu, Z. Sun, Enhanced Thermoelectric Performance of GeTe-Based Composites Incorporated with Fe Nanoparticles, ACS Appl. Mater. Interfaces 14(34) (2022) 38854-38864.

[13] Q. Zhang, M. Yuan, K. Pang, Y. Zhang, R. Wang, X. Tan, G. Wu, H. Hu, J. Wu, P. Sun, High-Performance Industrial-Grade p-Type $(Bi,Sb)_2Te_3$ Thermoelectric Enabled by a Stepwise Optimization Strategy, Adv. Mater. 35(21) (2023) 2300338.